Physics of a magnetic barrier in low-temperature bounded plasmas: insight from particle-in-cell simulations

2012 Plasma Sources Sci. Technol. 21 025002

(http://iopscience.iop.org/0963-0252/21/2/025002)

Plasma Sources Sci. Technol. **21** (2012) 025002 (14pp) doi:10.1088/0963-0252/21/2/025002

Physics of a magnetic barrier in low-temperature bounded plasmas: insight from particle-in-cell simulations

St Kolev[1], G J M Hagelaar[2], G Fubiani[2] and J-P Boeuf[2]

[1] Faculty of Physics, Sofia University, 5, J. Bourchier Blvd., BG-1164 Sofia, Bulgaria
[2] LAboratoire PLAsma et Conversion d'Energie (LAPLACE), Université de Toulouse, Bt. 3R2, 118 Route de Narbonne, F-31062 Toulouse Cedex 9, France

E-mail: skolev@phys.uni-sofia.bg

Received 14 August 2011, in final form 6 December 2011
Published 1 March 2012
Online at stacks.iop.org/PSST/21/025002

Abstract
The use of magnetic fields is quite common in low-pressure, low-temperature, gas-discharge devices for industrial applications. However, transport in such devices is still not very well clarified, mainly due to the presence of walls playing a crucial role and to the variety of configurations studied. The latter often obstruct the underlying basic physical phenomena and make the different studies valid only for very specific configurations. This work presents a numerical study of particle transport in low-pressure (0.3 Pa) plasmas across a localized transverse magnetic field (magnetic barrier) by means of the 2D3V particle-in-cell with Monte Carlo collisions method. The problem is treated as generally as possible while trying to reveal the basic physics, using very simplified chemistry and considering a simple rectangular configuration. The conditions chosen for the magnetic field are common to many applications—magnetized electrons and almost unmagnetized ions. Two basic configurations with different magnetic field directions are analyzed in detail: magnetic field perpendicular to the simulation plane and along the simulation plane. An extensive parametric study is carried out in order to obtain the main trends and scaling laws for particle transport with respect to different parameters: plasma density, magnetic barrier size and magnetic field magnitude. The total current of electrons crossing the barrier is found to scale linearly with the plasma density, which extends the validity of the obtained results to a wide range of plasma density values.

(Some figures may appear in colour only in the online journal)

1. Introduction

The problem of electron transport across a transverse magnetic field is rather old and has been studied for many years with respect to nuclear fusion devices based on magnetic confinement, probe diagnostics, particle beams, etc. In the last few decades, low-temperature plasma sources (LTPS) have found numerous applications and become an important part of the whole industry. There are several low-pressure plasma sources operating with magnetic fields (such as magnetron discharges, electron cyclotron resonance (ECR) plasma sources, Hall effect thrusters, end-hall sources and negative ion sources) and for them the problem of magnetized plasma transport is essential. While the magnetic field in these plasma sources is usually much lower compared with fusion devices and thus the ions are weakly magnetized, because of the relatively low gas pressure (below a few Pa), the electrons are still strongly magnetized and transport in the direction perpendicular to the magnetic field lines may pose problems similar to fusion plasmas. An important difference between LTPS and fusion devices however is that in most LTPS the vacuum chamber and geometry determine the discharge operation. The walls cause the formation of wall sheets which may interact with the magnetic field and produce additional transport. This effect appears to be especially important in devices where the magnetic field is used to reduce the electron transport in a certain direction.

The purpose of this work is to study electron transport across a localized magnetic field (also called magnetic barrier, MB) in the presence of chamber walls by means

of particle-in-cell (PIC) kinetic modeling. This work aims to give a better understanding of the influence of the walls on the electron transport in low-pressure LTPS and gives the trends in the scaling of electron transport with respect to different parameters such as the magnetic field strength, electron density, MB width (MB length which is to be traversed by the electrons) and the distance between the walls. These results are part of the authors' efforts [1–3] devoted to modeling negative hydrogen ion sources used in the neutral beam injection systems of fusion devices [4]. In these sources a magnetic field (magnetic filter) is used [5–7] to reduce the electron temperature and electron transport toward the extraction grid in order to increase the negative ion production and to allow their extraction.

Over the last two decades these sources have been extensively studied both theoretically and numerically. Although there are numerous works studying the problem of MB (also called magnetic filter) and the negative ion extraction system, none of them considers in detail the effect of cross-field transport caused by the chamber walls. In [8] the extraction physics is studied under realistic conditions using the 2D3V particle-in-cell with Monte Carlo collisions (PIC-MCC) method, but due to the high density only a single aperture is considered and the side walls of the real source are replaced by periodic boundary conditions. In [9] again the 2D3V PIC method is used to describe a bounded domain (including side walls); however, the magnetic field is chosen to have components only in the simulation plane, and thus the authors exclude any cross-field transport caused by the combined effect of the wall sheath/presheath and the magnetic field ($E \times B$ drift). Several works address the problem using the fluid approach [2, 10, 11]. While careful construction of fluid models could provide reasonable and qualitatively accurate results, they face serious difficulties related to boundary conditions and nonlocalities of low-pressure discharges. Therefore, this work presents an extended study of the MB problem and uses an explicit PIC-MCC method for the modeling.

While negative ion sources are the main motivation for this work, the results obtained are not limited to negative ion sources and might be useful for a broad range of plasma sources using magnetic fields. The problem is treated in a rather general way by considering the MB in very simplified geometry and plasma chemistry in order to exclude any effects specific to certain complex geometry or chemistry. Although geometry/chemistry effects may sometimes play a significant role, we think that the basic physics should be well understood first and should then be analyzed with respect to any specific configuration and additional effects should be added. Therefore, the geometry used here is a simple rectangle, the MB has an idealized Gaussian shape and the discharge is sustained by artificial charged particle injection and electron Maxwellization in a limited region.

This paper has the following structure. In the next section we recall some basic laws which are well known from the classical textbooks on plasma physics but we add them here explicitly to make the paper easier for reading. Next we briefly present the numerical model based on the PIC-MCC method and the conditions used in the simulations. In section 4 of the paper we present and analyze four simple configurations with different directions of magnetic field perpendicular to the plasma flow and different boundary conditions at the side walls—dielectric and grounded side walls. Here, we analyze the MB performance for reducing the electron flow toward the downstream region (to be defined precisely in section 4) where we apply certain attracting (extraction) positive potential. Section 5 includes several parametric studies of the plasma and MB characteristics with respect to different parameters: the plasma density, filter width and magnetic field strength. In section 6 we present the results of the variation of plasma parameters as a function of the transverse size of the domain (here in the 'y' direction) and their convergence to the 1D solution (where the side wall influence is neglected). Here we will also briefly comment on the excitation of instabilities leading to the so-called anomalous transport across the MB.

2. Basic laws

In the presence of a magnetic field the *motion of a single charged particle* (between collisions with other particles or walls) is described by the Newton equation:

$$\frac{\mathrm{d}\boldsymbol{v}}{\mathrm{d}t} = \frac{q}{m}(\boldsymbol{E} + \boldsymbol{v} \times \boldsymbol{B}), \tag{1}$$

where $\boldsymbol{v}$ is the particle velocity, q is the particle charge, m is the particle mass, $\boldsymbol{E}$ is the electric field and $\boldsymbol{B}$ is the magnetic field induction. Although precise (for single collisionless particle trajectory), the Newton equation is not convenient for the description of overall particle motion. For example, if the particle is gyrating in the magnetic field it could happen that on average it is not moving at all. Therefore, particle motion in a magnetic field (for weakly varying electric and magnetic fields) is usually considered as a sum of two components—fast gyration of the particle in a cyclotron orbit $x_{\mathrm{L}}(t)$, $v_{\mathrm{L}}(t)$ and slow drift ($x_{\mathrm{gc}}(t)$, $v_{\mathrm{gc}}(t)$) of the guiding center obtained after averaging out the cyclotron motion: $x(t) = x_{\mathrm{gc}}(t) + x_{\mathrm{L}}(t)$, $v(t) = v_{\mathrm{gc}}(t) + v_{\mathrm{L}}(t)$. With respect to the MB problem, we are mainly interested in the particle's guiding center motion, i.e. the particle drifts. In most of the plasma physics introductory textbooks one can find a detailed explanation of the different particle drifts (see for example [12, 13]). Here we will mention just those appearing for the field and geometry configurations considered in this work (assuming weakly varying fields):

$$\boldsymbol{v}_{E\times B} = \frac{\boldsymbol{E} \times \boldsymbol{B}}{B^2} \qquad E \times B \text{ drift}, \tag{2}$$

$$\boldsymbol{v}_{\nabla B} = \frac{q}{|q|}\frac{1}{2} v_{\perp} r_{\mathrm{L}} \frac{\boldsymbol{B} \times \nabla \boldsymbol{B}}{B^2} \qquad \nabla B \text{ drift}, \tag{3}$$

where r_{L} is the Larmor radius and $v_{\perp}$ is the magnitude of the velocity component perpendicular to the magnetic field. Of course one should remember that single particle motion has one more very important feature: collisions. This effect, however, is difficult to write using a simple formula for a single particle due to its random nature. Therefore, the phenomenon

is usually described with a statistical approach considering the averaged (collective) motion of many particles.

The *collective motion* of particles in a plasma is fully characterized by the Boltzmann equation or its moments. Within the drift–diffusion approximation the steady-state momentum equation is

$$n_s \boldsymbol{u}_s + \boldsymbol{\Omega}_s \times (n_s \boldsymbol{u}_s) = \frac{q_s}{|q_s|}\mu_s n_s \boldsymbol{E} - \nabla(D_s n_s) \equiv \boldsymbol{G}_s \quad (4)$$

where $\boldsymbol{G}_s$ is the drift–diffusion particle flux *without a magnetic field* for the species 's', $\boldsymbol{u}_s$ is the mean velocity, n_s is the species density,

$$\boldsymbol{\Omega}_s = \frac{q_s}{|q_s|}\mu_s \boldsymbol{B} = \frac{q_s}{|q_s|}\frac{e}{m_s \nu_{\mathrm{m},s}}\boldsymbol{B}$$

is a Hall parameter vector which represents the Hall parameter ($|\boldsymbol{\Omega}_s| = \Omega_s = \frac{q_s}{|q_s|}\mu_s|\boldsymbol{B}| = \frac{\omega_{\mathrm{c},s}}{\nu_{\mathrm{m},s}}$) along the different space dimensions, $\omega_{\mathrm{c},s} = (|q_s|B)/m_s$ is the cyclotron frequency of species 's', μ_s is the species mobility without a magnetic field, D_s is the diffusion coefficient without a magnetic field and $\nu_{\mathrm{m},s}$ is the momentum transfer collision frequency of species 's'. By applying cross and dot products with $\boldsymbol{\Omega}$ to equation (4) we obtain the drift–diffusion expression for charged particle flux in a plasma with a magnetic field [2]:

$$\boldsymbol{\Gamma}_s \equiv n_s \boldsymbol{u}_s = \frac{1}{1+\Omega_s^2}(\boldsymbol{G}_s + \boldsymbol{\Omega}_s(\boldsymbol{\Omega}_s \cdot \boldsymbol{G}_s) - \boldsymbol{\Omega}_s \times \boldsymbol{G}_s). \quad (5)$$

3. Numerical model and simulation conditions

The numerical model used here is an explicit PIC-MCC model [14–16]. The model is 2D in the configuration space and 3D in the velocity space (2D3V). The method used is based on the classical leap-frog Buneman–Boris algorithm scheme [14]. The PIC-MCC numerical technique provides the solution of the Boltzmann equation for the considered species and thus provides an accurate distribution function and resolves the full plasma dynamics. The major drawback of the explicit PIC-MCC method compared with the fluid approach is the considerable computational resources required for plasmas with high density in two and three spatial dimensions. In practice, this limits the modeling to plasmas with electron densities (n_e) in the order of $n_\mathrm{e} = 10^{14}$–10^{15} m^{-3} if we want to use a regular computer workstation. A further increase in the density would require a large-scale computer cluster or a supercomputer for the domain size considered in this work. At first glance, it appears that the PIC-MCC method would not be suitable for numerical modeling of most of the plasmas of practical interest, with densities usually from $n_\mathrm{e} = 10^{15}$ m^{-3} up to $n_\mathrm{e} = 10^{19}$ m^{-3} (the latter is the maximum value for high-power negative ion sources [4, 7]). However, one important observation found here allows us to use the PIC-MCC method at low densities and claim the validity of the obtained results for higher densities as well; the electron transport characteristics across the MB discussed in this work appear to scale linearly with the electron density. This will be shown in detail in section 5, subsection 5.1.

The species considered in the simulations are electrons (e), positive hydrogen ions (H^+) and hydrogen atoms (H).

Table 1. Collision processes.

Reaction number	Process	Reference
(1)	e + H → e + H (elastic)	[17, 18]
(2)	e + H → e + H* (five energy levels including the ionization process taken as an excitation)	[19]
(3)	H^+ + H → H^+ + H (elastic)	[20]
(4)	H^+ + H → H + H^+ (charge exchange)	[20]

Table 2. Common external simulation parameters.

Description	Symbol	Value
Gas pressure	p	0.3 Pa
Gas temperature	T_H	1000 K
Maxwellization temperature	T_M	6 eV
Gas density	N_H	2.17×10^{19} m^{-3}
Upstream wall potential ($x = 0$)	Φ_1	0 V
Downstream wall potential ($x = x_{\max}$)	Φ_2	25 V
Standard deviation	σ_B	1 cm

The last of these are assumed to have a homogeneous density (N_H) which is calculated from $N_\mathrm{H} = p/\kappa T_\mathrm{H}$, where p is the gas pressure, κ is the Boltzmann constant and T_H is the gas temperature in 'K'. The species composition is intentionally simplified in order to omit any additional effects due to more complex plasma chemistry. The processes taken into account and the sources for the cross-sections are summarized in table 1.

The main external parameters (discharge conditions) used within the simulations are denoted in table 2. The gas pressure is relatively low (0.3 Pa) and corresponds to the typical values in high-power negative hydrogen ion sources [7]. The low gas pressure leads to a mean free path of the electrons in the order of 20–50 cm, and 5–10 cm for the ions. The low pressure and the relatively small MB width considered here (around 2 cm for most of the simulations) mean that for a magnetic field of 5 mT the electrons are highly magnetized (Larmor radius 0.1–0.2 cm) and the ions are weakly magnetized (Larmor radius 2–4 cm).

The geometry considered in the simulations is a 2D rectangle (see figure 1). Most of the real sources with magnetic field are 3D systems and often without any symmetry axis/plane. Therefore, 2D modeling of such devices is an approximation assuming that along a certain dimension the size of the device will be very long. Here we consider two basic cases corresponding to two extreme cases—that the device is very long along the magnetic field direction and very long in the direction perpendicular to both the magnetic field and the plasma flow. The reality will be somewhere in between and will be an interplay of both.

In addition, usually in negative ion sources there is a plasma grid [7] (or here, the downstream wall), the first electrode of which is biased at the plasma potential or slightly higher in order to allow optimal negative ion extraction. Although negative ions are not included here, we use 'extraction' in order to have similar conditions and to obtain

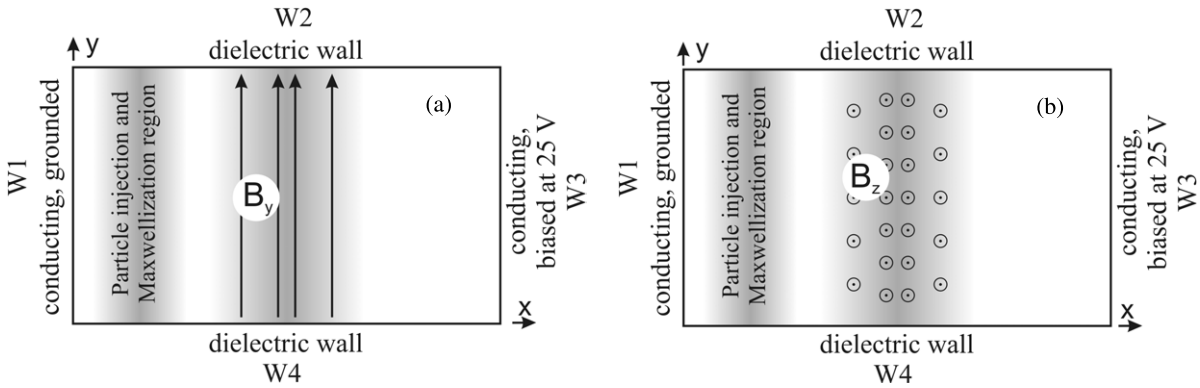

Figure 1. Schematic representation of the geometry and field configuration for the two modeled cases: (*a*) case D1 with $\boldsymbol{B} = (0, B_y(x), 0)$ and (*b*) case D2 with $\boldsymbol{B} = (0, 0, B_z(x))$. These figures are schematic representations of the configuration and do not correspond to the exact dimensions of the simulated cases which change throughout the paper.

the right behavior of the electrons which basically determine the overall plasma behavior due to the low electronegativity in these sources. By 'extraction' here we do not mean a full extraction system but just a simple positive bias applied at the downstream wall (see figure 1). Such a configuration does not exactly represent a real extraction system but it is sufficient to get a similar global potential and particle behavior without resolving the extraction holes. The bias value chosen here (25 V) is slightly higher than the peak plasma potential without any bias (determined by T_M and the geometry). Thus in the simulations, there is always a potential attracting the electrons crossing the barrier toward the downstream wall.

The magnetic field is directed along the 'z' or 'y' axis (see figure 1) with a Gaussian profile along 'x', centered at x_0:

$$B_{y,z}(x) = B_{y0,z0} \exp\left[-\frac{(x - x_0)^2}{2\sigma_B^2}\right]. \qquad (6)$$

In order to keep the model as general as possible, we specify no particular type of discharge. Instead, the plasma is sustained by artificial Maxwellization (the process of numerical enforcement of Maxwell distribution with a given temperature) of the electrons, and artificial injection of a constant number of charged particles in the upstream region. Although in this way the simulation is not completely self-consistent, this approach allows us to impose the electron temperature in the upstream region (defined roughly as $x \in (0, 4\,\text{cm})$) which facilitates the comparison of the different cases considered here. The Maxwellization and particle injection are performed in the region $x \in (0.5, 3.33)$ cm, i.e. outside the MB ($x < 3.33$ cm), so that they do not influence the electron transport in the MB and outside of the wall sheath near the left-hand side wall (W1, see figure 1) in order to allow undisturbed wall sheath formation. The latter is preferable if we want to have a potential barrier near the wall corresponding to the imposed electron temperature.

We use both Maxwellization and particle injection because with only one of them the model cannot reach a steady state. If we use only Maxwellization the temperature imposed on the plasma will be different from the self-consistent temperature, which will be able to sustain the discharge in a steady state. Therefore, the discharge will vanish if the imposed temperature is lower than the self-consistent temperature or the density will increase infinitely if it is higher. If we use only particle production/injection (with certain initial energies sampled from the Maxwellian distribution with certain temperature) we will face a situation where the high-energy electrons will be lost quickly on the walls but the low-energy particles will be held by the potential and thus the density will increase continuously (no steady state again). Therefore, both Maxwellization and injection are required to ensure the existence of steady state. Both procedures are described in detail in the appendix.

The explicit PIC method requires several conditions to be fulfilled for stable operation [14]. In the simulations carried out within this work we have the following conditions: $\Delta x/\lambda_D \approx 0.55$, $v_{th}\mathrm{d}t/\Delta x \approx 0.15$, $\omega_p/\mathrm{d}t \approx 0.06$, where Δx is the cell size, λ_D is the Debye length, $\mathrm{d}t$ is the time step, $v_{th} = \sqrt{2eT_e/m_e}$ is the electron thermal velocity (T_e in 'eV') and ω_p is the plasma frequency. The simulation time was up to 0.3 ms in order to reach the steady state.

4. Basic configurations of the magnetic barrier

In this section we present the results for simple square-shaped geometry and different directions of the magnetic field and the boundary conditions for the side walls. The left-hand side wall ($x = 0$) is conducting and grounded. The length of the walls is $L_x = L_y = 10$ cm. The charged particles are injected and Maxwell distribution is enforced in the region $x \in (0.5, 3.33)$ cm according the 'sine' distribution (equations (A.1) and (A.2) in the appendix) of the event frequency. The MB is positioned in the middle of the domain $x_0 = 5$ cm; it has a Gaussian distribution along 'x' (equation (6)) with $\sigma_B = 1$ cm and is homogeneous along 'y'. The magnetic field is always perpendicular to the main plasma flow direction (along x), i.e. we have only 'B_z' or only 'B_y' components of the magnetic field with $B_{z0} = 5$ mT and $B_{y0} = 5$ mT, respectively. The right-hand side wall ($x = 10$ cm) is biased with 25 V. The left-hand side region $x \in (0, 4)$ cm will be further denoted as the upstream region with the right-hand side $x \in (6, 10)$ cm as the downstream region. The side walls ($y = 0$ cm or $y = 10$ cm) are dielectric or conducting and will be further denoted as 'D' configurations

(for dielectric) and 'C' configurations (for conducting). The D1 and C1 cases will correspond to the magnetic field directed along the 'y' axis and D2 and C2 cases will correspond to the magnetic field directed along the 'z' (perpendicular to the simulation plane).

4.1. Dielectric side walls

In this subsection we analyze two basic cases: with the magnetic field directed toward the side walls (figure 1(*a*)) $\boldsymbol{B} = (0, B_y(x), 0)$, denoted as configuration D1, and the magnetic field directed perpendicular to the plane of simulation (figure 1(*b*)), i.e. $\boldsymbol{B} = (0, 0, B_z(x))$, which will be denoted as configuration D2.

Configuration D1: bounded plasma infinite in 'z' (figure 1(a)). The magnetic field has B_y component only: $\boldsymbol{B} = (0, B_y(x), 0)$, $\boldsymbol{E} = (E_x, E_y, 0)$, domain: $L_x = L_y = 10\,\text{cm}$.

For this configuration we have the following drifts allowed in the system

Single particle drifts (equations (2) and (3)):

$$\boldsymbol{v}_{E\times B} = (0, 0, E_x/B_y) \qquad \text{'}z\text{' component only,} \tag{7}$$

$$\boldsymbol{v}_{\nabla B} = \left(0, 0, -\frac{q}{|q|}\frac{1}{2}v_\perp r_L\frac{\nabla_x B_y}{B_y}\right) \qquad \text{'}z\text{' component only.} \tag{8}$$

The guiding center particle drifts are in the 'z' direction only where we have assumed infinity. This means that there are no particle drifts along 'x' and thus we should not expect any other type of transport across the barrier except due to collisions.

Collective motion drifts (equation (5)):

$$\Gamma_x = \frac{G_x}{1+\Omega^2}, \qquad \Gamma_y = G_y, \qquad \Gamma_z = \frac{\Omega}{1+\Omega^2}G_x. \tag{9}$$

As with the separate particle drifts, the collective particle drifts along 'x' are due to 'classical' collisional particle diffusion in the magnetic field [12, 13]. The particle flux is reduced due to the magnetic field as $1/(1+\Omega^2)$ and the MB is characterized by high stopping power for the electrons. We recall that this configuration approximately corresponds to the 1D case considering the transport across the barrier while the other dimensions are assumed to be infinite [3].

Configuration D2: bounded plasma infinite in 'z' (figure 1(b)). The magnetic field has B_z component only: $\boldsymbol{B} = (0, 0, B_z(x))$, $\boldsymbol{E} = (E_x, E_y, 0)$, domain: $L_x = L_y = 10\,\text{cm}$.

Single particle drifts (equations (2) and (3)):

$$\boldsymbol{v}_{E\times B} = (E_y/B_z, -E_x/B_z, 0) \qquad \text{'}x\text{' and '}y\text{' components,} \tag{10}$$

$$\boldsymbol{v}_{\nabla B} = \left(0, \frac{q}{|q|}\frac{1}{2}v_\perp r_L\frac{\nabla_x B_z}{B_z}, 0\right) \qquad \text{'}y\text{' component only.} \tag{11}$$

Here the $E \times B$ particle drift (E_y/B_z) allows transport across the barrier.

Collective motion drifts (equation (5)):

$$\Gamma_x = \frac{1}{1+\Omega^2}(G_x + \Omega G_y), \quad \Gamma_y = \frac{1}{1+\Omega^2}(G_y - \Omega G_x), \quad \Gamma_z = 0. \tag{12}$$

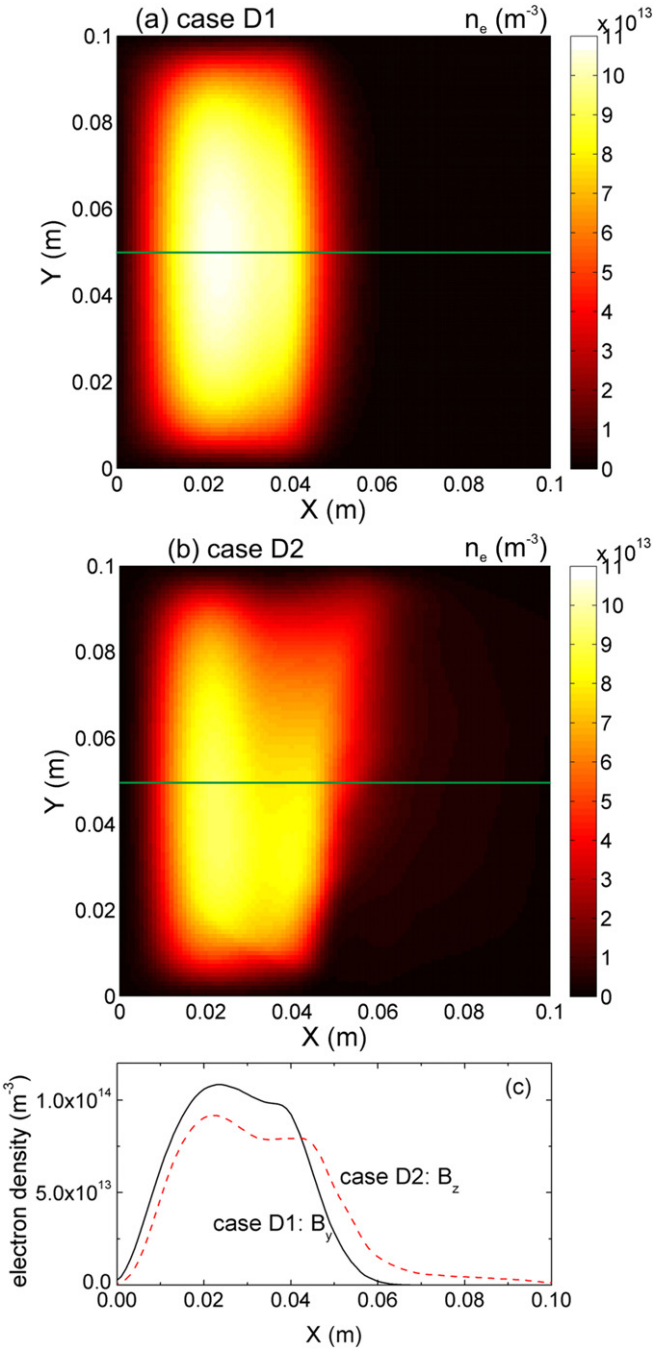

Figure 2. Electron density (m^{-3}) distribution for both configurations as they are denoted in the figure. Below: (*c*) a cross-section at $y = L_y/2 = 0.05$ m, in the middle of the domain shown with green line in (*a*) and (*b*).

The electron flux across the barrier Γ_x has two components, due to collisions $(G_x/(1+\Omega^2))$ and $(\Omega G_y/(1+\Omega^2))$ related to the $E \times B$ and diamagnetic drifts.

The results for the main characteristics in both cases (D1 and D2) will be presented in the next five figures which will be done by making a parallel between both cases for every plasma characteristic—potential, density, fluxes, etc. Figures 2 and 3 present the results for the electron density and electric potential distribution. Configuration D1 with B_y field apparently does not allow for significant transport

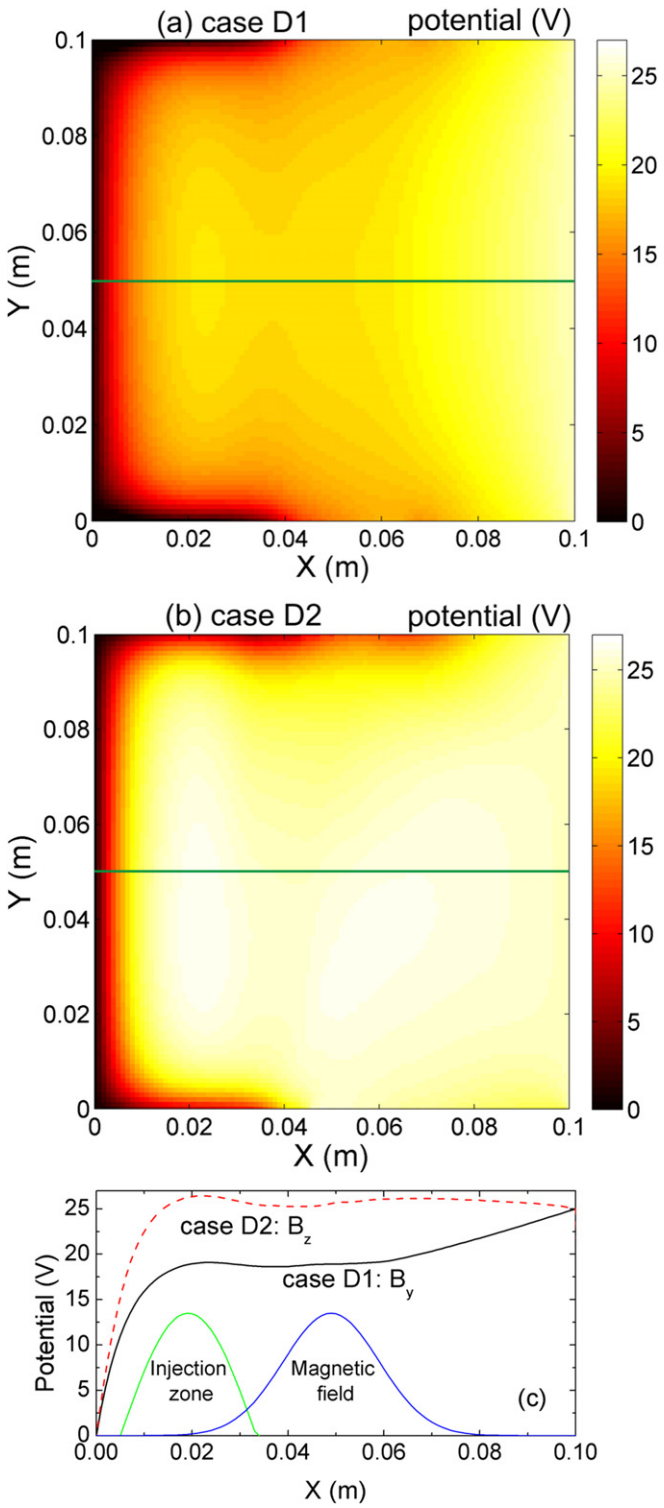

Figure 3. Electric potential (V) distribution for both configurations as they are denoted in the figure. Below: (*c*) a cross-section at $y = L_y/2 = 0.05$ m, in the middle of the domain shown with green line in (*a*) and (*b*). In (*c*) the shape and positions of the particle injection and Maxwellization zones are also shown.

across the barrier and provides symmetric density and potential distribution (figures 2(*a*) and 3(*a*)). A magnetic field strength of 50 G is enough to magnetize the electrons for the current conditions and thus to make the collisional transport across the barrier negligible. The barrier becomes a good 'isolator' and the bias at the extraction wall (W3) does not influence the upstream potential, which is determined by the electron temperature and the size of the upstream region. In the D2 case the $\boldsymbol{E} \times \boldsymbol{B}$ drift leads to significant losses across the barrier and thus to a reduction in the density (figure 2(*b*)) and an increase in the potential (figure 3(*b*)) in the upstream region. The potential profile cross-sections (figure 3(*c*)) clearly show an important difference between both—due to the relatively bad 'isolation' provided by the barrier in the D2 case, the extraction potential (25 V) penetrates significantly and the upstream potential is forced to increase above that value in order to preserve the plasma quasi-neutrality. With respect to negative ion sources with low electronegativity (like the H^- sources), the potential profile is a crucial factor and is still determined by the electron dynamics. If one needs to extract negative ions, they (the negative ions) should 'see' an attracting potential, i.e. the potential should increase toward the extraction wall (grid). Obviously, case D2 does not fulfill this condition and does not allow negative ion extraction with the chosen bias value. The bias has to be increased further in order to form an attracting potential profile. In contrast, configuration D1 provides an increasing potential toward W3 and thus allows for efficient negative ion extraction. Therefore, in general, if a high reduction in the electron current is required, the system should mimic the D1 configuration—with the magnetic field perpendicular to the wall in close proximity and the other side walls (in the 'z' direction) relatively far in order to reduce the effects of the $\boldsymbol{E} \times \boldsymbol{B}$ drifts.

The differences in the considered configurations result in differences in the electron temperature spatial distribution (figure 4). The temperature calculation here is based on the random motion energy, i.e. the directed motion energy is subtracted from the temperature calculation. Similarly to the density and potential, the temperature in configuration D1 (figure 4(*a*)) has a symmetrical distribution concentrated in the upstream region. In the downstream region there is no plasma in practice for D1 (see figure 2(*c*)). For configuration D2 the temperature distribution extends toward the downstream region near the upper side wall (W2), where the $\boldsymbol{E} \times \boldsymbol{B}$ drift toward the downstream wall is considerable.

The higher plasma penetration in this case is also well seen from the cross-section of the electron temperature plot (figure 4(*c*)). The temperature in the MB (figure 4) in D2 is considerably higher than the D1 case. Figure 5 represents the electron fluxes in both cases by overlapping the electron flux stream lines (white lines) and the flux magnitude (the color surface). While the D1 case has an ordinary pattern corresponding to the particle creation and heating in the upstream zone, the D2 case shows a much more complicated behavior. It appears that, in the upstream region, the electrons circulate in a counter-clockwise direction, enter the filter at the lower wall (W4), then penetrate the downstream region at the upper side wall (W2) and circulate in the downstream region in a clockwise direction. While this behavior makes sense from a fluid point of view, it is a bit unexpected if we consider it from the particle point of view. In the next subsection we will analyze the obtained results in detail. The ion flux distribution and stream plots (not shown here) show a pattern typical of

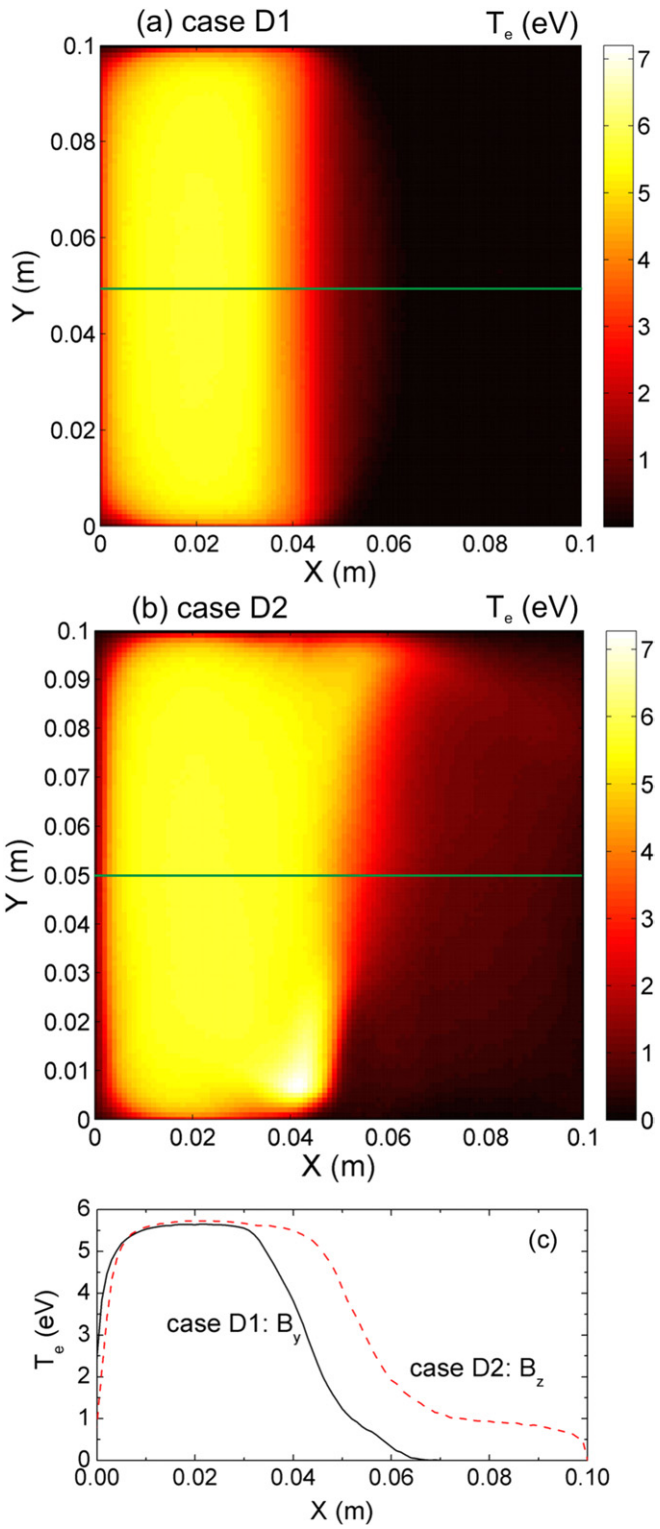

Figure 4. Electron temperature (eV) distribution for both configurations as they are denoted in the figure. Below: (*c*) a cross-section at $y = L_y/2 = 0.05$ m, in the middle of the domain shown with green line in (*a*) and (*b*).

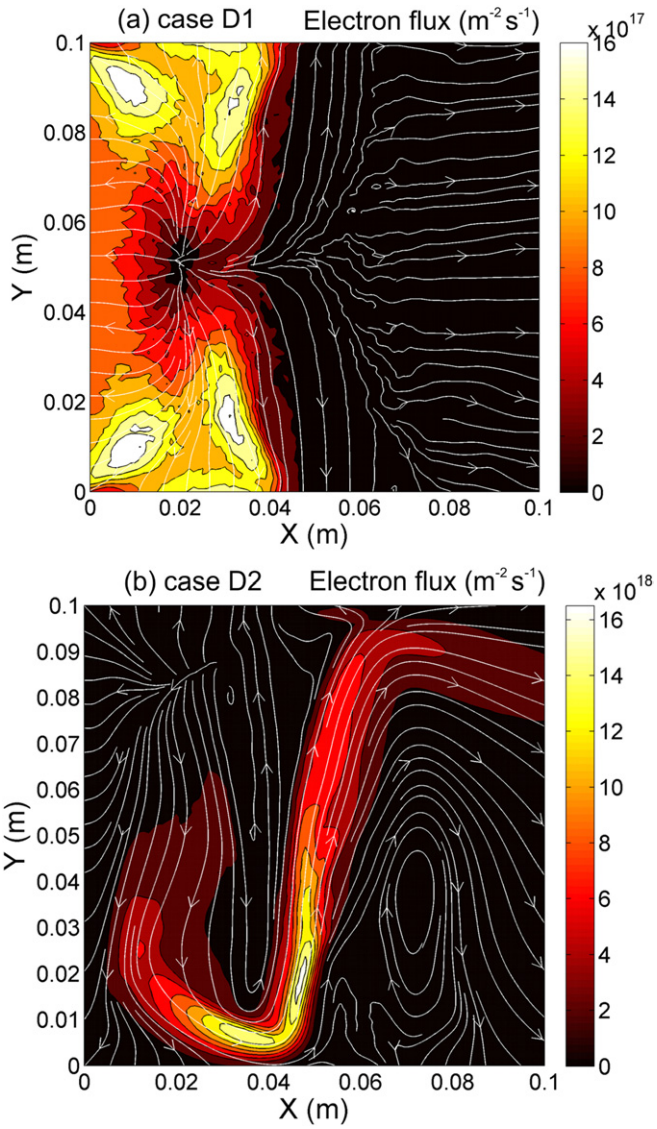

Figure 5. Electron flux ($m^{-2}\,s^{-1}$) distribution: The color corresponds to the flux magnitude and the stream lines correspond to the flux direction.

a plasma without a magnetic field. The reason for this is the weak magnetization of the ions because the ion Larmor radius is larger than the MB size.

The differences in the electron flux distribution in both cases result in a rather different distribution of the electron losses at the walls (figure 6). In the D1 configuration the electron and ion losses (not shown here) are mainly in the upstream region—the electrons are detained in the upstream region due to the MB and the ions due to the high positive bias at the downstream wall (W3). In the D2 case a considerable part (figure 6) of the electrons are lost in the downstream region at the extraction wall (W3) due to the $\boldsymbol{E} \times \boldsymbol{B}$ leakage and the attracting bias at W3, while the ion wall losses (now shown) are slightly altered compared with D1, due to the different potential distribution (figure 3). We recall that W1 wall is grounded and therefore at steady state the total electron and ion current (flux) at W1 and W3 should be equal. There is, however, no requirement to have ambipolar diffusion, i.e. equal local values of the electron and ion fluxes.

4.2. *Qualitative electron transport analysis*

Before continuing further with the presentation of results we would like to briefly discuss the plasma/particle transport for

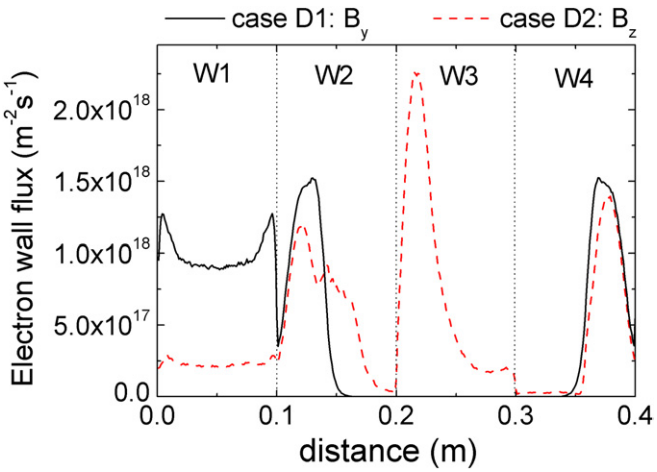

Figure 6. Electron wall flux distribution. The figure starts (distance = 0 m) at the lower left corner of the domain and continues up–right–down–left. Distances 0 m and 0.4 m are the same points.

the considered configurations. The discussion is based on well-known laws and does not represent new physics, but we find it useful for a better understanding of the results presented in this work. The D1 configuration has collisional transport only across the MB and thus it gives a rather simple and straightforward behavior. Therefore, we will focus our attention on D2 only. As already mentioned, for this configuration the particles have $E \times B$ drift with 'x' and 'y' components and ∇B drift with 'y' component only. This results in the following picture for the particle motion in the domain (see figure 7(a) presenting parts of real particle trajectories from the simulations). The electrons are injected in the upstream region with random velocity direction and thus most of them will move toward the MB—one part of them directly and the other part after reflection from the wall potential at W1. When they reach the barrier, due to their v_x velocity component they will be subjected to a Lorentz force pushing them in the positive 'y' direction, i.e. $v = (v_x, 0, 0) \Rightarrow \boldsymbol{F}_\mathrm{L} = (0, F_y, 0) \cong (0, ev_xB_z, 0)$ and thus increasing their v_y velocity component (in the positive direction). Having considerable positive v_y velocity results in a negative Lorentz force ($\boldsymbol{F}_\mathrm{L} \cong (-ev_yB_z, 0, 0)$) in the '$x$' direction, which will push them back in the upstream region as shown in figure 7(a). On average this motion will lead to a counter-clockwise circulation of the electrons in the upstream region, observed also in figure 5(b) (on average this produces a diamagnetic drift upward). This behavior, however, will be typical of electrons which do not have considerable initial negative v_y velocity. If they have, their v_y velocity in the barrier will not become positive and the electrons cannot return to the upstream region. If an electron enters the barrier near the upper wall W2 (in the wall sheath) it will have a significant $E \times B$ drift velocity $v_{E\times B}$ due to the strong positive electric field E_y and thus it will be able to cross the barrier (figure 7(a)). If it enters the barrier slightly below (in the presheath [21]) the $E \times B$ drift will be weaker and thus the ∇B drift will also influence the trajectory. In any case, the electron will probably cross the barrier in a trajectory similar to that shown in figure 7(a). A close examination of the 'x' component of the electron flux

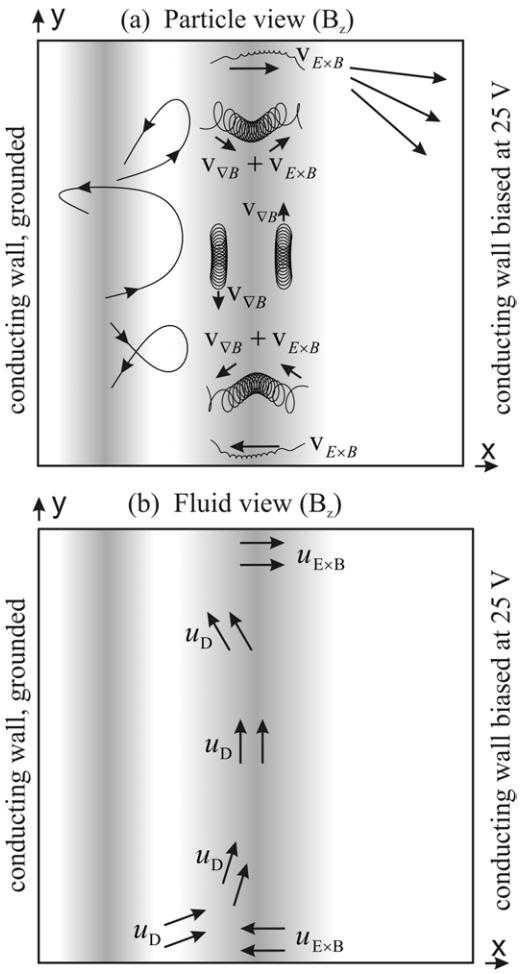

Figure 7. Particle (a) and fluid (b) view on the electron flux formation.

near the walls reveals that in fact the electron transport in the sheath itself does not give rise to a major contribution to the total electron current, but that the electron transport happens mainly in the presheath (plasma bulk near the wall but outside the sheath). There, the electric field is weaker than in the sheath but the higher density and larger area lead finally to a higher flux. Due to the flux complexity near the walls (figure 5) we cannot give an exact number of sheath and presheath contributions to the overall current. If an electron enters the barrier near the center without being reflected, it will be a subject of negative ∇B drift only because $E_y \approx 0$ in that area.

There is a certain probability that the electrons entering the downstream region will not be lost at the biased wall (W3). They could then go back to the upstream region at the lower half ($y < 4$ cm) of the MB due to the negative $E \times B$ drift. They also could be reflected by the magnetic field resulting, on average, in a clockwise circulation in the downstream region (observed also in figure 5(b)). And finally, the particles can enter the MB and cross it due to collisions (not shown in figure 7).

The above picture of particle motion, however, does not fit very well with the average (directed) electron motion in the MB seen in figure 5(b). It appears that the electron flux enters the barrier at the lower side wall (W4), moves up in the barrier (in the positive 'y' direction, perpendicular to the B_z field) and

then goes out of the barrier and enters the downstream region at the upper side wall (W2). Both 'points of view' (particle and collective) agree that the electrons will enter in the upstream zone at W2 but disagree as to where the electrons will enter the barrier. To understand why, we need to analyze the electron flux components (equations (12)).

In addition to the collisional transport (diffusion), there are two more components: $E \times B$ and diamagnetic drifts (figure 7(*b*)). The first one ($E \times B$ drift velocity, $\boldsymbol{u}_{E\times B} \propto (\boldsymbol{E} \times \boldsymbol{B})$) is a direct result of the averaging of the $E \times B$ drift of the separate particles. The diamagnetic drift, however, (diamagnetic velocity, $\boldsymbol{u}_{\mathrm{D}} \propto -(\nabla p \times \boldsymbol{B})$, where p is the pressure) has no particle analog and is a fluid-only drift (i.e. it is a result of averaging). This is a result of the density and temperature gradients (i.e. pressure gradient). The diamagnetic drift is not necessarily due to real drifts of particles (see [12, 13]). Even if there are no guiding center drifts of the particles, but there is a gradient of the density or temperature, the diamagnetic drift will be present. So the high value of the flux (directed velocity) magnitude in the MB (see figure 5(*b*)) may not correspond to real particle drifts! This is partially the case here. Figure 5(*b*) shows peak electron flux around the point $y = 0.02$ m, $x = 0.047$ m (the lower end of the barrier) directed upward (positive 'y'). However, the allowed particle drifts at this point are ∇B and $E \times B$ pushing the particles together downward and toward the upstream region (see figure 7(*a*)). The particles are allowed to move upward only due to collisions, but this effect is relatively weak. So despite the fact that the real drifts are directed toward the upstream zone and downward, the flux is directed upward ($u_{\mathrm{D},y} > 0, u_{\mathrm{D},x} \approx 0$). This is due to the dominant diamagnetic drift at that point as a result of the large density (see figure 2(*b*)) and electron temperature (figure 4(*b*)) gradients. Thus, the obtained flux pattern in the MB does not exactly represent the real particle drifts, but a flux due to averaging. The above picture is verified by close trajectory examination at the considered point. This, however, does not mean that the diamagnetic flux is spurious. As already mentioned, the particles coming from the upstream region and facing the magnetic field also contribute to the diamagnetic drift. The ∇B drift of separate particles is missing [12, 13] in the fluid plasma representation and does not have a direct fluid analog. However, as shown in [22], the diamagnetic drift and pressure gradient of charged particles are related to the magnetic field inhomogeneity and particularly to ∇B^2, which leads to a relation between the particle pressure and the magnetic pressure (proportional to B^2).

Apparently, the $E \times B$ drift in configuration D2 compromises the electron-stopping ability of the barrier. The current (mainly due to $E \times B$ drift) in D2 is three orders of magnitude higher than the drift due to collisions (12.2 mA for D2 against 0.0105 mA for D1, ratio = 1160). To fix this, we need to make the plasma configuration closer to D1, i.e. to build D2 with very large L_y. In this way the $E \times B$ current could become comparable to and even smaller than the collisional current across the barrier. This is studied in section 6 of this paper. However, this is usually not a practical method due to the unacceptable length of the device. Another popular method is to completely remove the $E \times B$ drift across the barrier by building the discharge configuration with closed $E \times B$ drifts [23]. The idea is simple—instead of making L_y very long let us wrap around the geometry. In cylindrical coordinates, the magnetic field will be in the radial direction and due to the axial symmetry no azimuthal electric field should exist. Any axial electric field (through the MB) will cause an azimuthal $E \times B$ current flowing in a closed loop, i.e. without crossing the barrier. Some devices such as Hall thrusters [24] and cylindrical magnetron discharges [25] use this effect to reduce the transport across the MB. However, it should be noted that such devices may be subjected to significant instabilities causing transport across the magnetic field, i.e. anomalous transport [26].

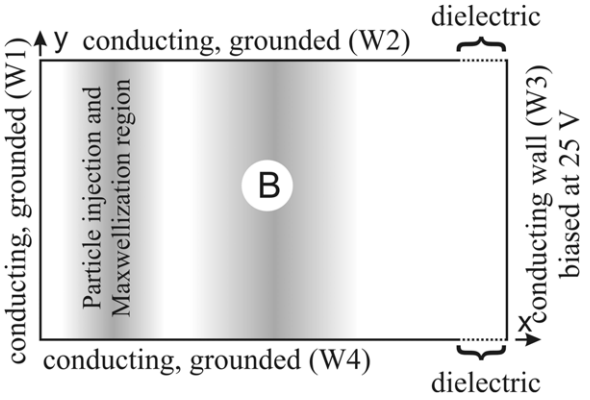

Figure 8. Schematic representation of the geometry and field configuration for the cases (C1 and C2) with conducting side walls.

4.3. Conducting (and grounded) side walls

For the sake of completeness we study a similar configuration but with conducting and grounded side walls (figure 8). We consider again two basic cases with perpendicular direction of the magnetic field: $\boldsymbol{B} = (0, B_y(x), 0)$ denoted as configuration C1 and $\boldsymbol{B} = (0, 0, B_z(x))$ denoted as C2. The conducting parts of the side walls are separated from the biased wall (W3) by a 1 cm dielectric (figure 8) in order to avoid sharp potential variation and thus strong electric fields.

A configuration with conducting walls generally allows highly nonambipolar plasma diffusion which may change the overall picture of electron and ion losses. Indeed, all plasma parameters are slightly altered but the general picture with respect to the MB operation is not considerably changed, and the results are qualitatively similar to the cases with dielectric walls. Therefore, we will not present a full set of results similar to the dielectric side wall cases, but only the results where significant differences are observed. Figure 9 presents the potential distribution for the C2 configuration. It is worth noting that for both configurations with grounded side walls (C1 and C2) the peak potential value in the upstream region is lower than the corresponding cases with dielectric side walls (see figures 3 and 9).

The reason for the relatively small differences between the dielectric and grounded side wall cases is that the electron drifts across the barrier are not related to the nature of the walls, but to the fact that the walls (regardless of their type) introduce

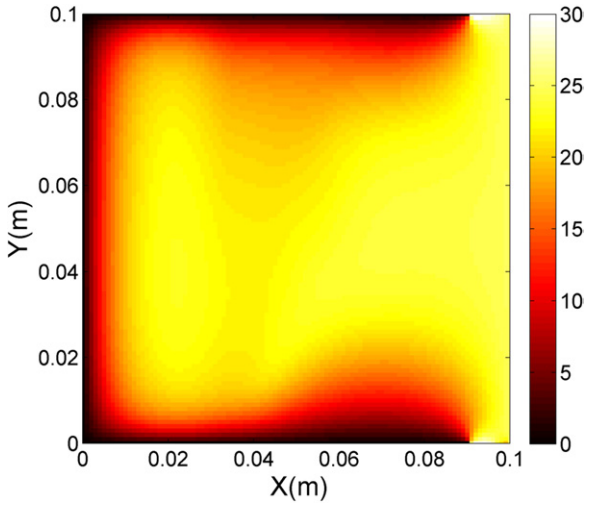

Figure 9. Electric potential (V) distribution for case C2 (B_z magnetic field).

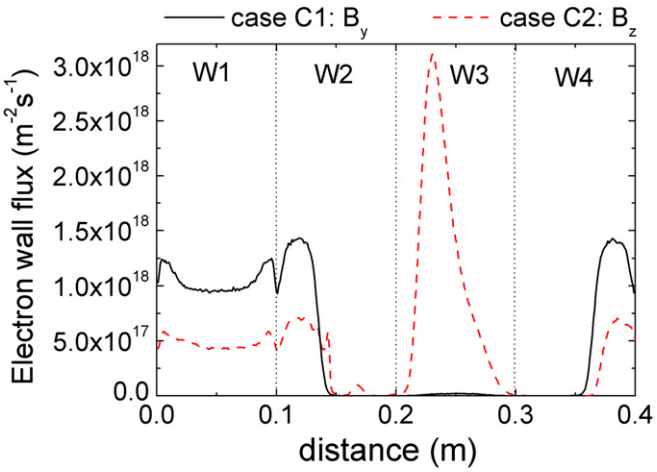

Figure 10. Electron wall flux distribution for the configurations with grounded side walls. The figure starts (distance = 0 m) at the lower left corner of the domain and continues up–right–down–left. Distances 0 m and 0.4 m are the same points.

particle losses and form a wall sheath/presheath that reflects the particles from the walls. Of course the sheath/presheath is slightly different in the two cases and this leads to the observed differences, particularly in the extracted current (see the next section).

Figure 10 shows the electron losses at the walls. The concept of Simon diffusion (reduced confinement due to short circuit wall currents) [21, 27] is not directly applicable here because the plasma is created outside the magnetic field region. Therefore, we do not observe considerable electron losses at the walls facing the magnetic field, but instead throughout the upstream region and at the extraction wall, which attracts the electrons to the downstream region.

5. Scaling laws for configuration with $E \times B$ drift across the magnetic barrier (configurations D2 and C2)

In this section we study the scaling of the MB performance with respect to several different parameters: electron density,

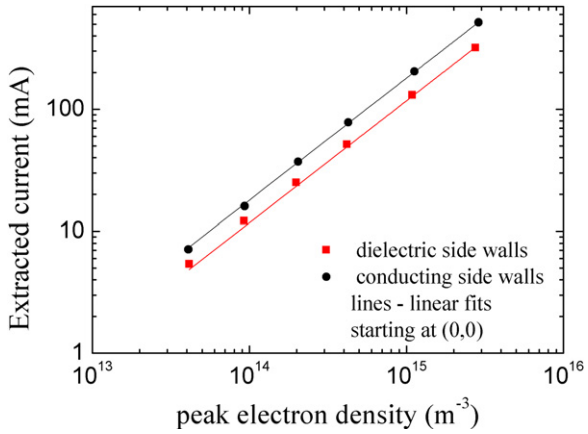

Figure 11. Extracted electron current for different peak electron densities in the upstream region.

magnetic field intensity and barrier size along 'x'. We are mainly interested in how the total extracted electron current (I_{extr}) going through the MB and reaching the biased wall depends on these parameters. I_{extr} is determined by counting all electrons reaching W3 for every time step and dividing their charge by the time step. All results will be for configurations with $E \times B$ drift, i.e. D2 and C2. The D1 and C1 configurations have only collisional diffusion across the barrier where the trends will follow the 1D solution for the problem [3]. Therefore, we will not analyze D1 and C1 here.

5.1. Scaling with the plasma density

The plasma density in these simulations is changed by changing the particle injection rate and namely the parameter ν_{inj}. The plasma density is proportional to ν_{inj} and the rest of the plasma characteristics are the same as those for the C2 and D2 configurations used in section 4 (see the comments at the beginning of section 4). The Maxwellization frequency need not be changed because the increase in the electron density automatically increases the collision rate and thus the same percentage of electrons will collide every time step, thus preserving the same temperature and distribution function.

Generally speaking, the increase in the plasma density reduces the wall sheath thickness. However, with the electron temperature fixed the potential drop between the MB (domain) center and the side walls is preserved, which results in a similar $E \times B$ velocity on average and in linear dependence (figure 11) of the extracted current on the plasma density (or to the peak density), $I_{\text{extr}} \propto A\, n_0$, where A is a constant. The PIC simulations show (figure 11) that the relation is linear for two orders of magnitude variation of the density. There is no reason for the linear dependence to fail outside the simulated region of densities, unless some nonlinear processes start to play a very significant role in the discharge and the electron transport across the barrier. Such processes could be, for example, Coulomb (electron–ion) collisions or instabilities. The Coulomb collisions become important at high densities (in the order of 10^{18} m^{-3}) for low electron temperatures (i.e. in the MB) and they are expected to enhance the transport across the barrier due to increased collisional transport. The instabilities

are relatively weak for the considered configurations and they seem to give a small contribution (see section 6). In general, the instabilities are nonlinear phenomena and if they determine the electron transport across the barrier, it is not clear how the extracted current will scale with the plasma density.

Another possible issue related to the density scaling is the ratio between the Larmor radius and the sheath size. The question that arises is what will happen to the electron transport if the Larmor radius becomes larger than the Debye length, or even the sheath size ($r_L > \lambda_D$)? For a magnetic field of 5 mT the electron Larmor radius is in the order of 1 mm, and for the highest density case simulated here (peak electron density $3 \times 10^{15}\,m^{-3}$) the Debye length is in the order of 0.5 mm, i.e. $r_L > \lambda_D$. The linear dependence is apparently still satisfied. The reason for this is probably the following: (1) the electron transport in the sheath itself does not provide the major contribution to the total electron current, but the electron transport happens mainly in the presheath (see section 4.2). (2) Even if the transport in the sheath becomes significant and predominant under certain conditions, the r_L/λ_D ratio would still not affect the electron transport because what is important is whether or not the electrons are reflected by the sheath. If the particles are reflected they will contribute to the $E \times B$ drift having trajectories similar to those shown in figure 7(*a*) near the side walls. In the extreme case of a very thin sheath ($r_L \gg \lambda_D$ at a very high density) the reflection becomes a 'point' reflection from the wall, and trajectory becomes cycloid-like giving rise to the so-called 'paramagnetic drift' [22]. This gives the same effect as the $E \times B$ drift, forcing the particle to drift along the wall and to cross the MB. In fact any process (not only electrostatic) causing electron-wall reflection (change in the v_y velocity sign) will produce a paramagnetic drift.

The observed linear scaling of the extracted current with density is very important for our study, because it makes the results obtained in this work applicable to conditions with densities outside the simulated region, and thus applicable to a wider range of plasma devices.

5.2. Scaling with the magnetic field magnitude

In the current set of simulations, the magnetic field distribution remains Gaussian (equation (6)) and we change B_{z0} only. The rest of the simulation conditions remain the same as in configurations C2 and D2 used in section 4 (see the comments at the beginning of section 4).

The obtained results are presented in figure 12. For conditions ensuring that the majority of the electrons are magnetized, i.e. $\Omega_e \gg 1$ and $r_L \ll$ domain size (see section 2, equation (5)), the expected relation for current scaling with magnetic field is approximately $I_{extr} = A/B_{z,max}$ where A is a constant. This is basically the relation expected for the $E \times B$ drift (see equation (12)), i.e. we assume that it gives the major contribution to the total current. As can be seen from the figure, this relation is well satisfied for values above 3.5 mT. Below 3 mT the electrons are weakly magnetized and the relation is more complicated. It should also be noted that the $1/B$ relation is derived with a constant electron temperature assumption which is not exactly true for the real simulation.

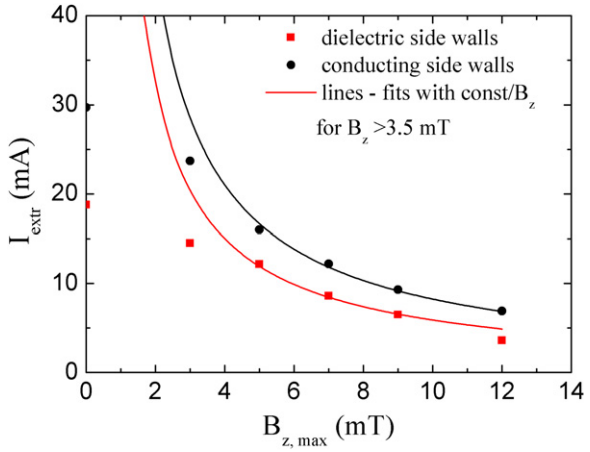

Figure 12. Extracted electron current as a function of the peak magnetic field strength. The lines represent fits with $I_{extr} = A/B_{z,max}$ using the results for $B_{z,max} > 3.5$ mT.

This could be a reason for certain deviation of the results from the $1/B$ relation.

5.3. Scaling with the magnetic barrier size along the magnetic barrier (along 'x')

In this series of simulations we consider a slightly modified geometry in which the domain size in the 'x' direction is larger: $L_x = 15$ cm, $L_y = 10$ cm. The domain is taken as larger in order to allow a larger MB width to be tested and to observe the system behavior as a function of significant variation of the considered parameter. The parameter varied here is the barrier length in the 'x' direction L_m (denoted as the 'barrier width'), i.e. along the plasma flow. As shown in figure 13(*a*), $L_m = 2$ cm corresponds to equation (6) (Gaussian distribution) with $x_0 = 5$ cm, $\sigma_B = 1$ cm. Larger barrier widths correspond to stretched versions of the Gaussian profile (see figure 13(*a*)). This approach provides a pulse-like shape for the magnetic field profile while preserving the same smooth fronts on both sides. The rest of the simulation conditions remain the same as in configurations C2 and D2 used in section 4 (see the comments at the beginning of section 4).

The extracted electron current decreases monotonically with the increase in L_m. Thus, the barrier width appears as another parameter giving a relatively simple way to enable additional reduction in the extracted electron current and thus increased barrier efficiency.

In all simulations the extracted electron current for configurations with conducting side walls is higher than the dielectric side wall cases. The different gradients of both curves (figure 13(*b*)) are probably related to the different potential profile established at the W2 wall along the MB. In the case of conducting side walls a higher potential barrier is established between the plasma and the side wall W2, thereby reducing the electron losses at W2, while they drift toward the extraction wall, enhancing the $E \times B$ drift. We would like to note that the results shown in figure 13(*b*) ($L_m = 2$ cm) do not match the results in figure 12 (5 mT) due to the different domain size in the 'x' direction used in the calculations.

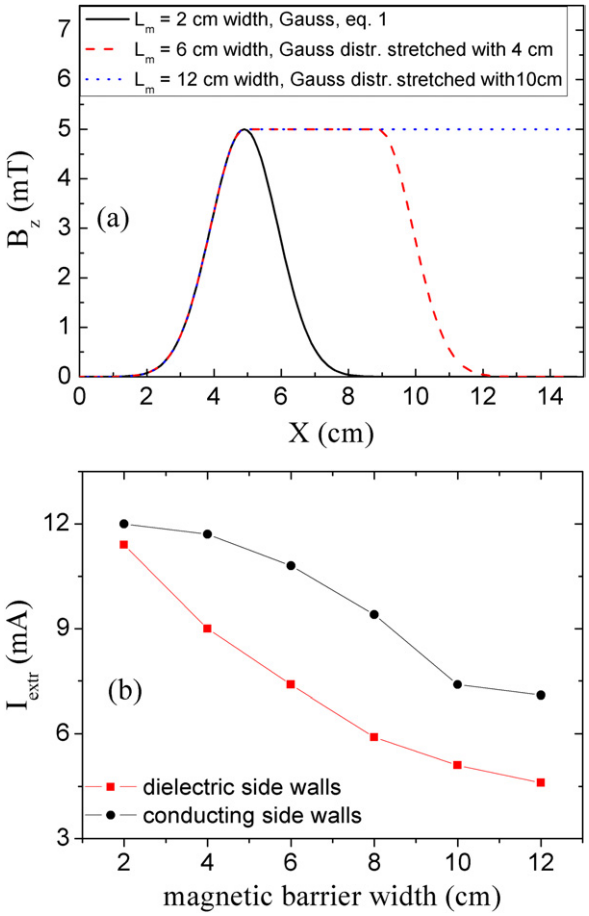

Figure 13. (*a*) Magnetic field profiles for three lengths of the MB; (*b*) extracted electron current as a function of the barrier width L_{m}.

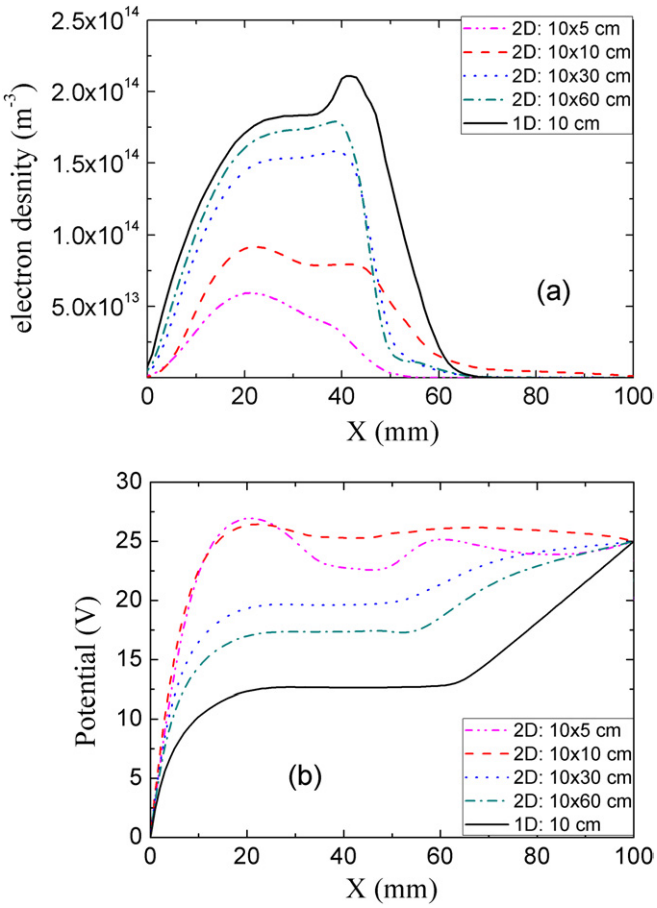

Figure 14. Cross-sections along 'x' at $y = L_y/2$ for configurations with dielectric side walls: (*a*) electron density; (*b*) electric potential. The 1D solution along 'x' for the same conditions is also shown.

6. Convergence to the 1D solution with the increase in the transverse domain size L_y

In this section we study the convergence of the 2D solutions to the 1D solution. By 1D solution we mean the solution along the 'x'-axis, with the domain lengths of the other axes ('y' and 'z') assumed to be infinite. In the 1D solution there is no $E \times B$ drift near the side walls because there are no side walls, and thus the particles cross the barrier due to collisions only. In principle, we expect to see convergence of the 2D solution as the transverse domain size L_y increases, thus approaching the infinity assumption.

Here we test several configurations similar to D2 but with a different size L_y. Except for L_y, the rest of the simulation conditions remain the same as in configurations C2 and D2 used in section 4 (see the comments at the beginning of section 4). Figure 14 shows the cross-sections of electron density and electric potential in the middle of the domain ($L_y/2$). The 2D solutions of density and potential clearly approach the 1D solution for large L_y. The density (at $L_y/2$) for the largest L_y becomes very close to the 1D solution, showing relatively weak influence of downstream extraction potential to the plasma in the upstream region. The lack of a well-pronounced density peak in the 2D solutions, compared with the 1D case [3], is due to the fact that in the latter the electrons have very long residence time in the MB (thus forming a peak

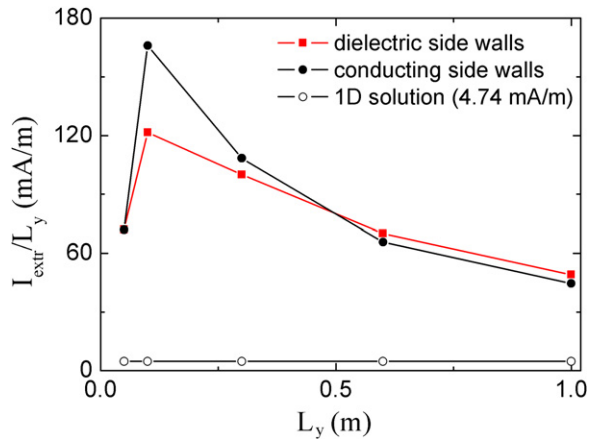

Figure 15. Extracted electron current as a function of the domain transverse size L_y. The 1D solution is also shown.

there). If we look at the extracted current (figure 15), there is a huge difference between the 1D solution and the largest L_y. In addition to the collisional and the $E \times B$ drifts, at relatively large L_y anomalous transport due to plasma instabilities starts to appear (figure 16). The instability forms plasma potential and density variations (wave) along the 'y'-axis. The presence of maxima and minima of the potential (figure 16(*b*)) means that there exists an E_y field causing $E \times B$ drift across the

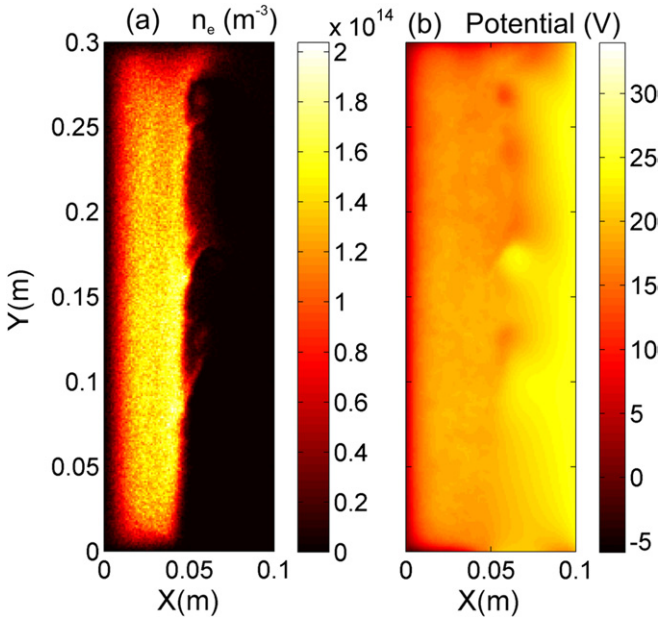

Figure 16. Color map of electron density (*a*) and potential (*b*) for a configuration with dielectric side walls and size $L_x = 10$ cm, $L_y = 30$ cm.

whole barrier (not only near the side walls), which gives rise to small spikes in the plasma density (figure 16(*a*)), formed by electrons crossing the barrier. The instability appears to be drift instability [12, 13] originating from the large temperature and density gradients across the MB (along 'x') causing a significant diamagnetic drift perpendicular to the magnetic field and thus drift waves propagating in the 'y' direction. From the results it follows that for the current configuration, even for $L_y = 1$ m the collisional and anomalous transport are responsible for less than 30% of the whole extracted current, and the main transport mechanism is still the $E \times B$ drift. The instabilities, their effect on the particle transport and their contribution to the overall current will be analyzed in detail in another paper.

Going back to figure 15 and the extracted current, we are not able to reach a long enough L_y where the total extracted electron current will be close to the 1D solution result. We expect that even at a very long L_y (several meters) they will not coincide completely due to the presence of anomalous transport.

7. Conclusions

This paper illustrates and quantifies the fact that in low-pressure, low-temperature plasma devices the walls play a very important role in the electron transport through a magnetic field. This is especially true in the case of the magnetic barrier used in negative ion sources for neutral beam injection in fusion devices. In such devices, the localized plasma source (producing plasma outside the MB) creates an electron pressure (p_e) gradient which leads to a $\nabla p_e \times \boldsymbol{B}$ drift (diamagnetic drift) that tends to turn around the source region (diamagnetic current). If there is no wall perpendicular to the $\nabla p_e \times \boldsymbol{B}$ current then there is a closed drift current. However, if the $\nabla p_e \times \boldsymbol{B}$ current goes to a wall as in the negative ion source (and in configurations D2 and C2), then part of the current is redirected by the wall, due to the $E \times B$ drift associated with the field in the presheath between the plasma and the wall (the sheath gives a relatively small contribution). As a result, the electron current through the perpendicular magnetic field is significantly enhanced by the side walls, if the magnetic field is perpendicular to both the plasma flow and to the electric field formed near the walls (wall sheath and presheath), regardless of the wall material (conducting or dielectric). At low gas pressures the electron transport through the MB is dominated by this drift and it is orders of magnitude higher than the electron collisional transport (calculated from the C1/D1 cases).

In this work we have performed a broad parametric study giving the scaling of electron transport for different discharge characteristics: plasma density, magnetic field magnitude, magnetic barrier size and domain size. The total current of electrons crossing the barrier is found to scale linearly with the plasma density, which extends the validity of the obtained results to a wide range of plasma density values, far beyond the attainable range with our numerical code and the available computer resources. The obtained electron scaling with the magnetic field strength ($I_{extr} \propto 1/B_z$) basically confirms the conclusion of dominant $E \times B$ drifts when the electrons are magnetized. Another parameter which also allows a reduction in electron transport (or enhancement of the barrier performance) is the magnetic barrier size along the plasma flow. The increase in the magnetized path for the electrons effectively reduces the total electron current, and thus together with the magnetic field strength gives two parameters, which could be relatively easily controlled to reduce the electron transport across the barrier.

Our attempt to reach or just approach the 1D solution by extending the transverse domain length shows that even for a large transverse size the $E \times B$ drift remains the primary reason for the electron transport (at least for the considered configuration and pressure).

Finally, we would like to note once again that although this study is initiated by negative hydrogen ion sources it gives the general behavior of plasmas in bounded configurations. It should also be stressed that this work considers a low-pressure plasma, with gas pressure 0.3 Pa. Any increase in the pressure will proportionally increase the collisional transport (diffusion) and thus will make the $E \times B$ and anomalous drifts less important. For example, if we increase the gas pressure 20 times (up to 6 Pa), by looking at figure 15, roughly speaking, we can conclude that the collisional transport will become comparable to and even more important than the other types of transport. Thus the picture will be slightly different. The particular pressure values at which this becomes true will depend on the particular gas and discharge configuration.

Acknowledgments

This work was carried out within a Sofia University Grant no 24/13.04.2011. The authors from LAPLACE laboratory in Toulouse acknowledge support from the French National

Research Agency (ANR ITER-NIS, BLAN08-2 310122) and from EFDA, CEA and the French 'Fédération de Recherche sur la Fusion'.

Appendix. Maxwellization and particle injection procedures

The *electron Maxwellization* of electrons is done by virtual 'Maxwellizing collisions'. Every time step a certain number of electrons are picked up depending on the spatial profile of the collision probability we impose, and their velocity is changed by randomly sampling from isotropic Maxwellian distribution with temperature T_{M}. Therefore, the electron temperature in the upstream region never becomes exactly T_{M}, but slightly lower because there are always particles which are not Maxwellized in several time steps. Even if we significantly increase the rate of 'Maxwellizing collisions' the only consequence will be the fact that the electron temperature in the upstream region will be even closer to T_{M}.

Here we impose as an external parameter the 'Maxwellizing collision frequency' $\nu_{\mathrm{h}}(x, y)$. Once having the collision frequency spatial distribution we use the null collision method [16] to do the 'collisions'. Obviously, these are not real collisions but virtual collisions giving the electrons new velocities. The procedure is done in this way to be compatible with the rest of the Monte Carlo procedures.

The profile of the 'Maxwellizing collision frequency' is taken to have a half-period sine shape, i.e.

$$\nu_{\mathrm{h}}(x, y) = \begin{cases} 1 \times 10^7 \frac{\pi}{2} \sin\left(\pi \frac{x - x_a}{x_b - x_a}\right), & \text{if } x \in (x_a, x_b), \\ 0, & \text{if } x \notin (x_a, x_b), \end{cases} \quad \text{(A.1)}$$

where $x_a = 5 \times 10^{-3}$ m and $x_b = 3.333 \times 10^{-2}$ m.

The *particle injection* is done in a similar way. We impose as external parameters the 'injection collision frequency' $\nu_{\mathrm{inj}}(x, y)$ with a similar profile:

$$\nu_{\mathrm{inj}}(x, y) = \begin{cases} \nu_{\mathrm{inj}0} \frac{\pi}{2} \sin\left(\pi \frac{x - x_a}{x_b - x_a}\right), & \text{if } x \in (x_a, x_b), \\ 0, & \text{if } x \notin (x_a, x_b), \end{cases} \quad \text{(A.2)}$$

and certain 'target density' n_{inj}. Here $\nu_{\mathrm{inj}0} = 7 \times 10^5\ \mathrm{s}^{-1}$, $x_a = 5 \times 10^{-3}$ m and $x_b = 3.333 \times 10^{-2}$ m. The change in the electron (and ion) density due to injection is simply $\mathrm{d}n/\mathrm{d}t|_{\mathrm{injection}} = n_{\mathrm{inj}} \nu_{\mathrm{inj}}(x, y)$ and thus every time step we inject a constant number of particles in the domain, regardless of the real density of the different particle species. Both $\nu_{\mathrm{inj}}(x, y)$ and $\nu_{\mathrm{h}}(x, y)$ are uniform along the 'y' direction.

References

[1] Boeuf J P, Hagelaar G J M, Sarrailh P, Fubiani G and Kohen N 2011 *Plasma Sources Sci. Technol.* **20** 015002
[2] Hagelaar G J M, Fubiani G and Boeuf J P 2011 *Plasma Sources Sci. Technol.* **20** 015001
[3] Kolev St, Hagelaar G J M and Boeuf J P 2009 *Phys. Plasmas* **16** 042318
[4] Hemsworth R S and Inoue T 2005 *IEEE Trans. Plasma Sci.* **33** 1799
[5] Leung K N, Ehlers K W and Bacal M 1983 *Rev. Sci. Instrum.* **54** 56
[6] Bacal M 2006 *Nucl. Fusion* **46** S250
[7] Fantz U *et al* 2008 *Rev. Sci. Instrum.* **79** 02A511
[8] Taccogna F, Minelli P, Longo S, Capitelli M and Schneider R 2010 *Phys. Plasmas* **17** 063502
[9] Kuppel S, Matsushita D, Hatayama A and Bacal M 2011 *J. Appl. Phys.* **109** 013305
[10] Kolev St, Lishev St, Shivarova A, Tarnev Kh and Wilhelm R 2007 *Plasma Phys. Control. Fusion* **49** 1349
[11] Lishev St, Shivarova A and Tarnev Kh 2010 *J. Phys.: Conf. Ser.* **223** 012003
[12] Chen F 1984 *Introduction to Plasma Physics and Controlled Fusion* (New York: Plenum)
[13] Bellan P M 2008 *Fundamentals of Plasma Physics* (Cambridge: Cambridge University Press)
[14] Birdsall C K and Langdon A B 1985 *Plasma Physics via Computer Simulation* (New York: McGraw-Hill)
[15] Hockney R W and Eastwood J W 1989 *Computer Simulation Using Particles* (London: Taylor and Francis)
[16] Vahedi V and Surendra M 1995 *Comput. Phys. Commun.* **87** 179
[17] Itikawa Y 1974 *At. Data Nucl. Data Tables* **14** 1
[18] Trajmar S and Kanik I 1995 *Atomic and Molecular Processes in Fusion Edge Plasmas* ed R K Janev (New York: Plenum) p 40
[19] Janev R K, Reiter D and Samm U 2003 Collision processes in low-temperature hydrogen plasmas *FZ-Jülich Report* No 4105, http://www.eirene.de/report_4105.pdf
[20] Krstiæ P S and Schultz D R 1998 *Atomic and Plasma–Material Interaction Data for Fusion* vol 8 (Vienna: IAEA)
[21] Lieberman M A and Lichtenberg A J 1994 *Principles of Plasma Discharges and Materials Processing* (New York: Wiley)
[22] Golant V E, Zhilinsky A P and Sakharov I E 1980 *Fundamentals of Plasma Physics* (New York: Wiley) chapter 8.6
[23] Keidar M and Beilis I I 2006 *IEEE Trans. Plasma Sci.* **34** 804
[24] Goebel D M and Katz I 2008 *Fundamentals of Electric Propulsion: Ion and Hall Thrusters* (New York: Wiley)
[25] Levchenko I, Romanov M, Keidar M and Beilis I I 2004 *Appl. Phys. Lett.* **85** 2202–5
[26] Adam J C *et al* 2008 *Plasma Phys. Control. Fusion* **50** 124041
[27] Simon A 1955 *Phys. Rev.* **98** 317–8